Wind Speed Effects on Sea Surface Emission and Reflection for the Along Track Scanning Radiometer

PHILIP D. WATTS, MYLES R. ALLEN,* AND TIMOTHY J. NIGHTINGALE

Atmospheric Science Division, Rutherford Appleton Laboratory, Chilton, Oxon, United Kingdom

ABSTRACT

The emission and reflection properties of a rough sea surface are investigated, with particular emphasis on the wavelengths and viewing geometry relevant to the Along Track Scanning Radiometer. The authors start from Fresnel's equations for a flat water surface and calculate the effect of changing sea state on direct emissivity and reflectivity. The authors then investigate the role of surface-emitted surface-reflected (SESR) radiation, which enhances emissivity at high wind speeds. The effect of foam and whitecaps at high wind speeds is referred to briefly in the appendix but essentially remains an unknown quantity.

Radiative transfer calculations that employ emissivity models also have to consider the reflection of down-welling radiance from the atmosphere. Although energy conservation requires that reflectivity is 1 minus emissivity, the variability of the sky brightness with zenith demands that one consider also the angular distribution of the reflected radiance. Additionally, the extended statistical model is used to investigate what one may call surface-reflected surface-reflected (SRSR) radiance.

It was found that the SESR and SRSR effects, and the reflection of the anisotropic sky radiance, together act to cancel the first-order effect of reduced emissivity with increasing wind speed, such that the approximation of constant emissivity and specular reflection is essentially valid for the Along Track Scanning Radiometer viewing geometry. Finally, parameterizations are derived for the variable emission and reflection of a rough sea surface that are suitable for fast radiative transfer models.

1. Introduction

The emission and reflection properties of a rough sea in the 4- and 12-μm infrared sounding windows have been studied both theoretically and experimentally in some detail over the last 30 years. In particular, the pioneering work of Cox and Munk (1954), who measured the characteristic slope distributions of a wind-driven sea using aircraft observations of sun glitter, has provided the basis for many subsequent studies. Saunders (1968) performed comprehensive calculations based on geometrical optics and the Cox and Munk statistics, including the effects of shadowing, multiple surface reflections, and consideration of the anisotropy of the sky radiance. Results were obtained for view zenith angles from nadir to the horizon for the 8.5–12-μm region and showed that radiances observed from a rough sea would be *higher* than those over a calm sea. His calculations were confirmed by measurements made with a shore-mounted narrow-field-of-view radiometer. Despite, or perhaps because of, being comprehensive, Saunders does not provide detailed enough information to derive an emission and reflection model for the Along Track Scanning Radiometer (ATSR), hence the work presented here.

Other authors since Saunders have performed analogous or similar calculations. Notably Sidrin (1981) who calculates rough sea emissivities and reflectivies for a large range of wavelengths but does not include multiple reflection effects despite presenting results at high view zenith angles. Sidrin calculates the rough sea effect on reflection, that of spreading the range of contributing sky zenith angles around the specular direction, but considers the effect to be unimportant for sea surface temperature (SST) sounding. Masuda et al. (1988) calculate emissivity in the 3.5–4.1- and 8–13-μm window regions for all view angles but do not consider multiple reflections or rough sea reflectivity. Various authors have quoted or used the Masuda results in studies of the effect of emissivity on sea surface temperature retrieval. Coll and Caselles (1994) apply them to analysis of Advanced Very High Resolution Radiometer (AVHRR) SST retrievals and assume specular reflection. Otterman et al. (1992) use them but recognize that multiple surface reflections and anisotropic sky radiance may be significant without, however, going beyond a simple analysis. Francois and Ottle

---

* Current affiliation: Center for Meteorology and Physical Oceanography, Massachusetts Institute of Technology, Cambridge, Massachusetts.

Corresponding author address: Philip D. Watts, DRAL, Rutherford Appleton Laboratory, Chilton DIDCOT, Oxfordshire OX11 0QX, United Kingdom.

(1994) have confirmed the angular effect predicted by the Masuda results using ATSR-measured brightness temperatures. However, they did not proceed to study the wind speed effect, leaving this to a future paper. Harris et al. (1994) use the Masuda results to estimate wind speed effect on AVHRR and ATSR SST retrieval accuracy. They performed a simple analysis of the multiple reflection and sky radiance effects (A. Harris 1994, personal communication) and concluded they would not be significant.

In the microwave frequency region, the sea has a much lower emissivity than in the infrared, and consequently, the multiple reflection and sky radiation effects are noticably larger. They have therefore received more attention in the literature. Wilheit (1979) made use of the geometrical optics approach to emissivity calculation using the Cox and Munk statistics but with a reduced slope variance to account for the fact that, with long wavelength radiation, the smallest wave facets do not contribute to the slope distribution. He also did not consider the anisotropic sky radiance or multiple reflection effects. Wentz (1983) redressed some of this by proposing an effective, that is, enhanced, reflection coefficient parameterized in terms of the emissivity and the wind speed. Guissard and Sobieski (1987) improved upon this, noting that the enhanced reflection was also a function of the behavior of the zenith sky radiance that is in turn primarily a function of opacity or atmospheric transmittance. Guissard et al. (1993) continue on this theme and derive a reflection factor that they parameterize in terms of the channel total attenuation and a wind friction velocity. Petty and Katsaros (1993) take a different approach: they keep the reflectivity equal to 1 minus emissivity but apply it to sky radiance arriving, not at the specular angle, but at an effective (higher) zenith angle. These authors also address multiple reflections and find rather a small effect at the view angle they considered (53°), justifying their use of a somewhat simplified treatment over that taken in this paper.

In this paper we study the emission and reflection of a rough sea, including the effects of multiple reflection and anisotropy of sky radiance, with special regard to the viewing geometry of the ATSR instrument. Details of the ATSR instrument can be found in Edwards et al. (1990); however, a brief review of its relevant characteristics is warranted here. The ATSR is an infrared radiometer designed specifically to measure sea surface temperature from space to an unprecedented accuracy (<0.3 K) to meet the needs of the climate research community. To achieve this, a conical scan is employed resulting in two views of the same surface scene: a "nadir" view with a zenith angle at the surface of between 0° and 25°, and a "forward" view with a zenith angle from 52° to 55°. Upwelling radiance at wavelengths centered around 3.7, 11, and 12 μm (i.e., the usual "split" and "dual" windows) are measured at each view angle for a nominal surface pixel size of

approximately 1 km. (The forward view pixels are about twice as large because of the geometry.) Thus, the atmospheric effect on the radiances can be removed and the sea surface temperature measured by using both spectral and multipath information. The forward view angle was chosen after detailed simulations (Zavody 1994) to maximize the path difference of the two views without the forward view becoming totally opaque in tropical atmospheres and without it also being so large as to give rise to uncertainties in the sea surface emissivity. However, the emissivity does start to vary significantly with view angle for angles around and above 55° and becomes a function of sea state. We have performed this study because the high accuracy demanded of the sea surface temperature product from ATSR demands also that the emissivity is known to a high accuracy. Although various results are present in the literature on this subject, calculations specific to the ATSR geometry and including a detailed treatment of surface reflection effects are not available.

The Fresnel relations are applied to the rough sea as described by the Cox and Munk model, essentially to reproduce the results of Masuda et al. (1988). We then quantify the enhancement to emissivity caused by reflection of surface emitted radiation into the view direction making extended use of the Cox and Munk statistics and including shadowing effects in a manner similar to that of Saunders (1968). The zenith angle distribution of the reflected radiation and the total effect, but not angular distribution, of radiance reflected twice by the surface into the view direction are calculated. The emissivity and reflection calculations are used in conjunction with downwelling radiances calculated for all zenith angles to establish the importance of multiple reflections and the sky radiance anisotropy.

Finally, we present simple parameterizations of the rough surface emission and reflection suitable for use in fast radiative transfer models. For emission this consists of a quadratic fit of emissivity to wind speed and view angle. For reflection we parameterize a factor representing the increase in reflected radiance over the specular approximation in terms of the wind speed and the total channel transmittance.

2. Sea surface emission

The basic angular dependence of emissivity of a flat water surface is given by Fresnel's equations [see, e.g., Eqs. (2)–(4) of Sidrin 1981]. The emissivities of the individual polarizations change appreciably even at small angles, whereas the mean or total emissivity is roughly constant until zenith angles of 40°–50° when it starts to reduce with increasing rapidity, reaching zero at 90°. Emission at different wavelengths has similar behavior but different low-angle asymptotes.

a. Direct emission from a slope distribution model

Statistics of the sea surface were obtained by Cox and Munk (1954) using aircraft photographs of sun-
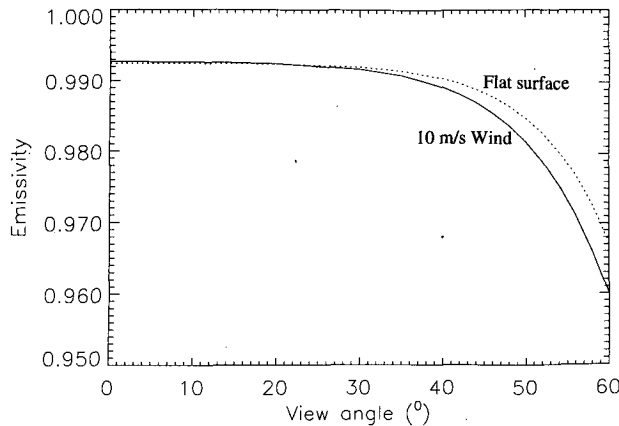
Fig. 1. The direct emissivity of a water surface at 11 μm as a function of viewing angle. The dotted line is for a plane surface and the solid line is for a rough surface resulting from a wind speed of 10 m s^{-1}.

glint. They showed that, to a good approximation, the distribution of slope angles found for a particular wind speed was Gaussian with a variance (in degrees squared) given by

$$\sigma^2 = 0.003 + 0.00512W \pm 0.004, \qquad (2.1)$$

where W (m s^{-1}) is the wind speed at a height of 12.5 m. Differences in the distribution with respect to the crosswind and upwind directions were found to be small and are ignored here. Sidrin (1981) gives results that show the orientation of the wind direction is not important for view zenith angles less than 70°. At low (i.e., close to normal) view angles, the effect of variable facet slopes is to include higher-angle facets and thus to reduce the emissivity below the simple Fresnel value. At high view angles, however, where shadowing occurs, the effect is to include low-angle facets and thus to increase the emissivity. At the ATSR forward view angle, that is, around 55°, the effect is a reduction of emissivity. We apply the Cox and Munk slope distributions following Eq. (18) of Masuda et al. (1988) that properly accounts for the distribution and the area projected by a facet in a particular view direction, $\mu = \cos(\theta)$, to obtain

$$\epsilon(\mu) = \frac{2}{\pi\sigma^2\mu} \int_0^1 \int_0^\pi \epsilon_F(\mathbf{n}, \chi)$$
$$\times \cos\chi \exp\left(- \frac{\tan^2\theta_n}{\sigma^2}\right) \mu_n^{-4} d\phi_n d\mu_n. \qquad (2.2)$$

Here subscript n refers to the facet normal vector making a zenith angle $\mu_n = \cos(\theta_n)$ and azimuth ϕ_n to the vertical. The exponential term is the Gaussian distribution of Cox and Munk; χ is the angle the facet normal makes with the view direction such that

$$\cos\chi = \cos\theta \cos\theta_n + \sin\theta \sin\theta_n \cos\phi_n. \qquad (2.3)$$

(See appendix A for a definition of the geometry used.) Finally, $\epsilon_F(\mathbf{n}, \chi)$, is the Fresnel emissivity of the facet at angle χ and complex refractive index $\mathbf{n}$. The value of $\mathbf{n}$ for an ATSR channel of finite bandwith is obtained using the filter response weighted mean wavelength as described in appendix B. For brevity, we hereafter drop the explicit reference to $\mathbf{n}$ where it appears in ϵ_F. For consistency, the integrated probability

$$p(\mu) = \frac{2}{\pi\sigma^2\mu} \int_0^1 \int_0^\pi \cos\chi \exp\left(- \frac{\tan^2\theta_n}{\sigma^2}\right) \mu_n^{-4} d\phi_n d\mu_n$$
$$(2.4)$$

should be equal to unity, but in practice it differed by around 0.003. This introduces significant errors into $\epsilon(\mu)$. Better numerical integration might improve this but it was found quite accurate to use $p(\mu)$ to normalize the result of (2.2). In this way agreement to within 1 part in 10^4 with Masuda's published results was obtained. Masuda also uses $p(\mu)$ as a normalization factor but at high view angles and for a different reason: to allow for facets "shadowed" because of their steepness. For ATSR-viewing geometries and reasonable wind speeds (where slopes greater than 40° remain improbable), shadowing is not a significant effect for the calculation of direct emission. We do, however, use $p(\mu)$ to normalize the integration in the presence of shadowing when we calculate $\epsilon(\mu)$ for high view angles [section 2a(2)].

First, we show, in Fig. 1, for the 11-μm channel, the emissivity against view zenith angle for a flat surface (dotted line) and a rough sea surface (solid line) corresponding to a 10 m s^{-1} wind. This shows the reduction in emissivity from the plane surface value due to sea state. It also allows us to conclude that for low zenith angles (less than 30°) there is no significant angle or wind speed dependence. Emissivity values for the ATSR nadir view can therefore be fixed at the plane
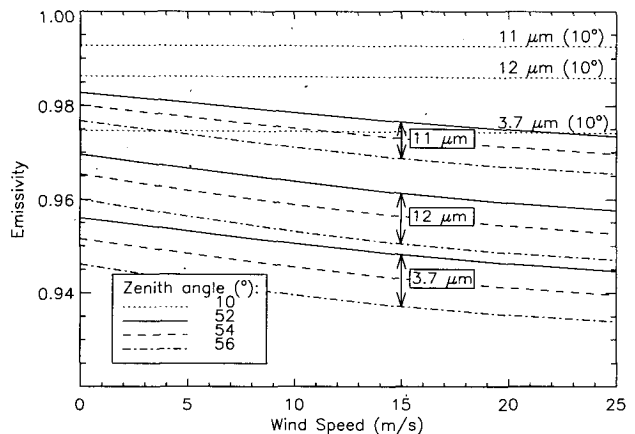

Fig. 2. The direct emissivity of a wind-roughened sea for the three thermal channels at nadir and forward viewing angles.

surface nadir values. Figure 2 concentrates specifically on the behavior at the ATSR view angles. It shows that there is a significant change of emissivity with windspeed at forward view angles and a lack of dependence at nadir angles. It also shows that there is a dependence on view angle even over the restricted range (52°–56°) observed in the forward view of ATSR.

b. Surface-emitted surface-reflected emission

When significant surface facet slopes (e.g., >10°) are present then radiance emitted at high zenith angles (i.e., toward the horizon) can be reflected into the satellite view direction. This is illustrated in the Fig. 3. The surface-emitted surface-reflected (SESR) effect is described by Otterman et al. (1992). They do not analyze it but state that the 13° mean slope present for a 10 m s^{-1} wind should give rise to SESR effects when the view zenith is greater than 50°. Saunders (1968) does account for SESR radiation in a much more complete manner but one that is still a slight approximation over the method presented below.

Referring to Fig. 3, we consider the emissivity at facet or surface B in the satellite direction (given by the vector $\mathbf{i}$) that makes an angle θ to the zenith and χ_B to the local vertical (given by $\mathbf{n}_B$). Radiance emitted from surfaces like A at the appropriate angle χ_A to the local vertical such that it arrives at surface B and reflects specularly into direction $\mathbf{i}$, is SESR radiance. Sky radiance arriving in direction $\mathbf{r}$ at A, undergoing specular reflection at A then B to leave also in direction $\mathbf{i}$, is surface-reflected surface-reflected (SRSR) radiance. We may write the radiance leaving surface B in direction i as a sum of emission and reflection terms; thus,

$$R_i = B_{\text{sea}}\epsilon_F(\chi_B) + [1 - \epsilon_F(\chi_B)]$$
$$\times \{B_{\text{sea}}\epsilon_F(\chi_A) + R_{\text{sky}}(\theta_r)[1 - \epsilon_F(\chi_A)]\}, \quad (2.5)$$

where the first term is the direct emission, the first term in the parentheses is the SESR emission, and the last term is the SRSR reflection. Here B_{sea} is the Planck emission at the sea temperature and R_{sky} is the downwelling-angle-dependent atmospheric radiance.

This section attempts to quantify the effect of SESR radiance to enhance the emissivity of the sea surface. Discussion of SRSR radiance, which acts in enhancing the reflectivity, is deferred until the general question of reflectivity is addressed.

The total effective emissivity of the facet $\epsilon'(\chi_B)$ $= R_{i(\text{emission})}/B_{\text{sea}}$ is therefore

$$\epsilon'(\chi_B) = \epsilon_F(\chi_B) + [1 - \epsilon_F(\chi_B)]\epsilon_F(\chi_A). \quad (2.6)$$

Detailed analysis of SESR effects is not possible, because although the Cox and Munk slope model characterizes χ_B, it does not provide information on χ_A that would need detailed information on the surface geometry. The approach taken here is to assume that the statistics of the sea slopes *as seen from any particular*
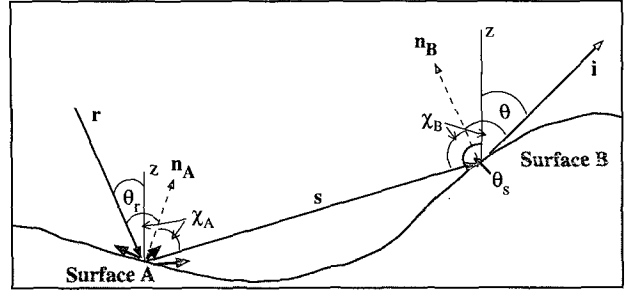

FIG. 3. Diagram to show the origin and geometry of direct and SESR emission and SRSR reflection.

facet are also described by the Cox and Munk model, and instead of the Fresnel emission of slope A, $\epsilon_F(\chi_A)$ in (2.6), we use the sea emission at the incidence angle $\pi - \theta_s$, $\epsilon(\pi - \theta_s)$. This is precalculated from (2.2) extending the range of calculation to zenith angles just below the horizon.

Thus, we assume that the effective facet emissivity can be written as

$$\epsilon'(\chi_B) = \epsilon_F(\chi_B) + [1 - \epsilon_F(\chi_B)]\epsilon(\pi - \theta_s). \quad (2.7)$$

Emissivity $\epsilon'(\chi_B)$ is then substituted for $\epsilon_F(\chi_B)$ into (2.2) to obtain the sea emission *including* SESR radiation. Saunders (1968) used the mean emission from normal and grazing angle viewing rather than the explicit emissivity at $\pi - \theta_s$; Petty and Katsaros (1994) used the emission from grazing angle viewing.

Caveats apply to this method. First, when calculating the emissivity from (2.2) at high zenith angles (greater than 55°), shadowing takes place. "First-order" shadowing, that is, facets that face away from the observer, are easily excluded from the integration since for these $\chi > 90°$. The fact that these facets shadow others and thus may change the slope distribution is not easily accounted for. Saunders assumes facets of all orientation are shadowed equally, which is equivalent to assuming that the distribution does not change.

Second, the Cox and Munk slope statistics are applicable to a large area of sea; the statistics of slopes in the field of view of one particular slope, for example, in the wave trough, may differ. Finally, because we specify a radiance field and not the actual sea surface emitting the SESR radiation, it is not easy to say at which point, when θ_s becomes less than 90°, the radiance emanates from the sky and not the sea. However, given a typical wave height/wavelength ratio, it is fairly easy to establish a crude cutoff angle that is probably better than assuming the value to be 90°. If the wave height is H and the wavelength is L, then the critical zenith angle, θ_{cutoff}, below which radiation originates from the sky not the sea is given by

$$\theta_{\text{cutoff}} = \frac{\pi}{2} - \tan^{-1}\left(\frac{2H}{L}\right). \quad (2.8)$$

TABLE 1. Characteristic wave heights H and wavelengths L in meters, and the corresponding θ_{cutoff}, for the wind speeds of the Beaufort scale (after Neumann 1954).

Beaufort force	1	2	3	4	5	6	7	8	9	10
Mean wind (k)	2	5	8	13	19	25	30	36	44	51
H (m)	0.011	0.055	0.182	0.55	1.30	2.50	4.50	7.00	11.0	15.8
L (m)	0.12	2	6	16	31	80	115	163	225	301
θ_{cutoff}	79.6	86.9	86.5	86.1	85.2	84.4	83.6	83.1	82.3	82.0

The parameter H/L is known as the "steepness" of the sea. Of course, the critical angle also depends on the location of the facet, for example, in a trough or on a peak, but we can attempt only a rough estimate of the cutoff angle. Stokes's theory provides the limit H/L < 0.142 (Michell 1893), implying θ_{cutoff} > 74°. More realistically, values of H/L lie between 0.1 and 0.008 (Kinsman 1984, p. 6), corresponding to angles of 79°–89.1°. The mean values of H and L in Table 1 for different Beaufort wind speeds are given in Neumann (1954). The corresponding θ_{cutoff} values are seen to be reasonably constant.

In the following analysis we perform the calculation of SESR radiation with cutoff angles of 90° and 85°: the 90° expected to give the minimum SESR effect and the 85° expected to give a realistic maximum effect.

The high zenith angle radiance/emissivity field for various wind speeds obtained by integration of (2.2) accounting for hidden pixels (and *without* SESR) is given in Fig. 4. The flat surface Fresnel emissivity steadily approaches zero at grazing incidence. With slopes present the emissivity falls to zero at higher zenith angles: when the steepest slopes (~35°) are just approaching grazing incidence, all others are hidden. The higher wind speeds produce more steep slopes, and hence, higher emissivity is maintained at the higher ze-

nith angles. As described earlier, this enhancement of emissivity is contrary to the behavior at lower zenith angles where the presence of slopes lowers the emissivity over the flat surface value. The crossover point can be just seen in Fig. 4 at about 68°. We should note that emissivities in Fig. 4 beyond 95° are not used with the cutoff angles used in this paper.

With these high-angle emissivities used through (2.7) in (2.2), we obtain the channel emissivities for 55° view zenith angle shown in Fig. 5. Clearly, the SESR radiation has a significant effect at winds speeds of 5–10 m s^{-1} and greater. The distinction between the result of assuming different horizons is fortunately not very marked.

3. Sea surface reflection

The total reflectivity of a rough sea follows directly from the total emissivity by energy conservation; that is, $\rho = 1 - \epsilon$. However, unlike the sea surface, which can be assumed to have the same temperature whatever the direction of the emitted radiation, the sky radiance will be more or less strongly dependent on the zenith angle depending on the opacity of the atmosphere. It is therefore necessary to ask not only what is the total reflectivity but also what is its angular distribution. For
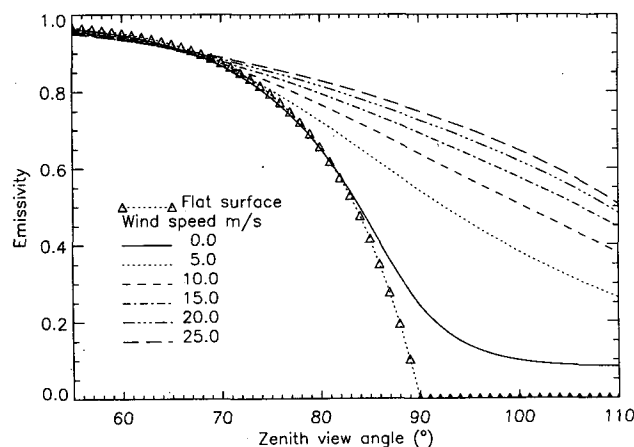

FIG. 4. The direct emissivity of a wind roughened sea for the 3.7-μm channel at view zenith angles from 55° to 110° and at various wind speeds. The values are obtained from integration of Eq. (2.2), excluding facets that are hidden from view.
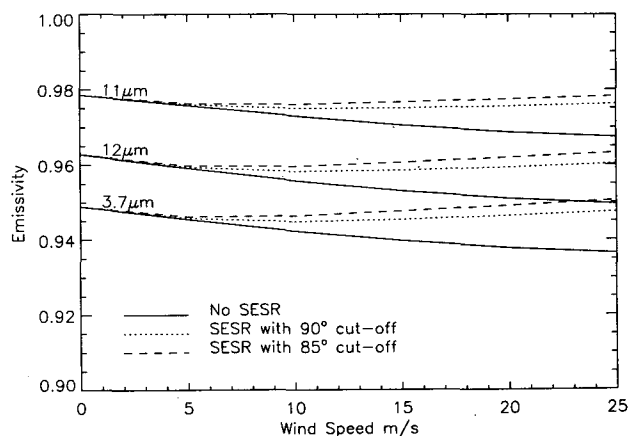

FIG. 5. The emissivity of a wind roughened sea for the three thermal channels at various wind speeds and at a forward view zenith angle of 55°. Three values are shown: the direct emissivity (no SESR) and the emissivities including the effect of SESR radiation with 90° and 85° cutoff horizons.
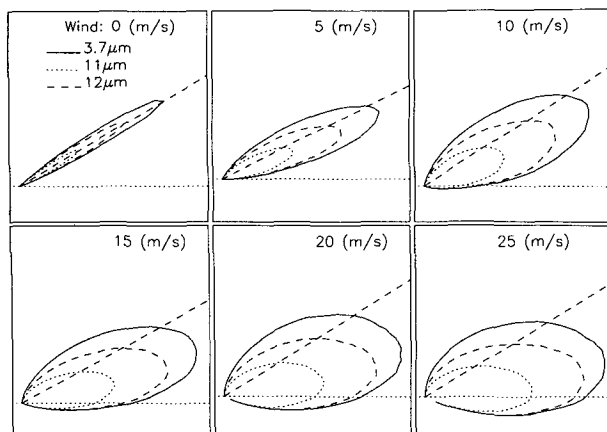
FIG. 6. Reflection lobes for the three thermal channels at the 55° view zenith and for various wind speeds obtained using Monte Carlo simulations. The three thermal channels are shown. Lines of constant reflectance are spaced at intervals of 2.5E-4 per degree (i.e., 0.025% per degree) and the zenith angle interval is 10°. The 55° forward view zenith angle used in the simulation and the specular reflection angle are shown by dashed lines. Two-hundred thousand random facets were used to provide the ensemble for the simulation.

clear skies, at least, and at infrared wavelengths, we can normally assume that the sky radiance is isotropic in azimuth so that only the zenith angle dependence is required. For a mirror surface the reflection is specular; the spread would be zero. As the surface roughens, the spread will increase, and we may also expect the mean angle to differ in some way from the view zenith because obliquely viewed facets will reflect more efficiently but with less projected area than acutely viewed facets.

We determined the sea surface reflectivity by a Monte Carlo method. Sea surface facets were generated with frequencies of slopes θ_n and azimuth ϕ_n in accordance with the Cox and Munk probability distribution. The resulting outgoing ray zenith and azimuth angles, θ_s and ϕ_s, were counted and weighted by the Fresnel reflectivity $[1 - \epsilon_F(\chi)]$ to give the distribution of outgoing rays, which, by reciprocity, is equivalent to the distribution of angles contributing to the reflection toward the satellite. A number of facets between 10^5 and 3×10^5, depending on the wind speed, were needed to adequately specify the distribution. A suitable check on the results of the Monte Carlo simulation is provided by stipulating that the total reflection is consistent with the emissivity calculated by the direct integration method.

Figure 6 shows the zenith angle dependence of the reflected rays for wind speeds from 0 to 25 m s^{-1} and 55° view angle. The direction of specular reflection is shown by a dashed line at 55°. It is clear that the reflection lobes are biased to a higher zenith angle than the specular direction, although the polar plot tends to hide the longer tail of the distribution at low angles. At

lower wind speeds the lobe is narrower and the mean angle is nearer the specular direction. Figure 6 shows that at 5 m s^{-1} there is practically no below-horizon radiation. The Cox and Munk formula predicts the presence of slopes at zero wind speed so that, even here, the reflection lobe is of finite width.

The presence of rays from below the horizon is consistent with the SESR radiation discussed in previous sections. It also suggests that we should be concerned with the problem of sky radiation reflected into the part of the lobe below the horizon, what we may call surface-reflected surface-reflected (SRSR) radiation. Although involving two reflections and only a small part of the lobe, the angles will be near grazing, and therefore, reflectivities will be high.

SRSR radiation is not easy to simulate even with Monte Carlo methods because of the double reflection. Being a small effect it is reasonable to expect it is not worth a detailed study. We can gauge at least the total magnitude of SRSR reflection by noting that, in the calculation of SESR radiation, if $\epsilon(\theta_s)$ is the high angle emissivity, then $1 - \epsilon(\theta_s)$ is the high angle reflectivity. Thus, in the integration of (2.2) we can replace $\epsilon_F(\chi)$ by

$$\rho_{SRSR}(\chi) = [1 - \epsilon_F(\chi)][1 - \epsilon(\pi - \theta_s)],$$

$$\theta_s > 90 \text{ or } 85° \quad (3.1)$$

to obtain the total SRSR radiation. We do not obtain the angular distribution, but, if the effect is small, it will be adequate to assume that the distribution is the same as that of the direct reflection lobe and simply add it to it. By formulating SRSR radiation in this way we also ensure energy conservation.

Results of the SRSR calculation are shown in Fig. 7. The labels refer to the channel and the cutoff angle for θ_s. As expected, the SRSR reflectivities are quite small, of order 5% of the direct reflectivities.
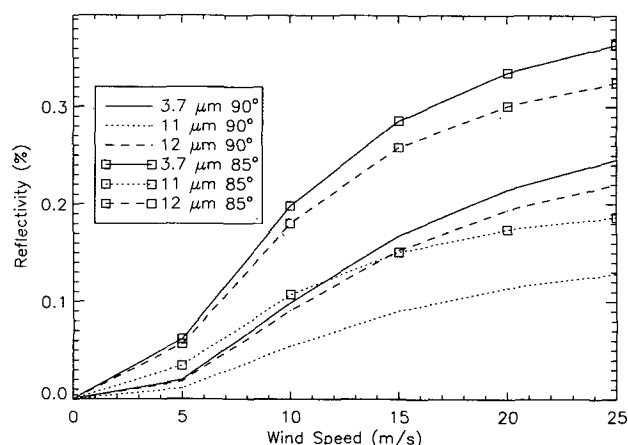

FIG. 7. The enhancement to reflectivity from SRSR radiation for the three thermal channels at the 55° forward view angle and the two horizon cutoff angles.

4. Summary of radiance terms

At this point we summarize the terms, both emission and reflection, derived in this paper. They are best described as two sets: those where the reflected ray arrives with zenith angle $\theta_s < \theta_{\text{cutoff}}$, that is, from above the horizon and those where $\theta_s > \theta_{\text{cutoff}}$. Although the distinction is meaningful only for the reflectivity and the SESR terms, it is kept anyway for the direct emissivity.

$\theta_s < \theta_{\text{cutoff}}$ (above horizon)

Direct emission: ϵ_A Fresnel emissivity ϵ_F integrated over part of the Cox and Munk facet distribution that gives $\theta_s < \theta_{\text{cutoff}}$. From (2.2).

Direct reflection: ρ_A Distribution given by Monte Carlo simulations.

$\theta_s > \theta_{\text{cutoff}}$ (below horizon)

Direct emission: ϵ_B Fresnel emissivity, ϵ_F, integrated over part of the Cox and Munk facet distribution that gives $\theta_s > \theta_{\text{cutoff}}$. From (2.2).

SESR emission: $\epsilon_{\text{SESR}} = (1 - \epsilon_F)\epsilon(\theta)$ integrated similarly; $\epsilon(\theta)$ is the high-angle emissivity field, that is, $\epsilon_A + \epsilon_B$ calculated over angles $\theta < \pi - \theta_{\text{cutoff}}$ with hidden facets removed.

SRSR reflection: $\rho_{\text{SRSR}} = (1 - \epsilon_F)[1 - \epsilon(\pi - \theta_s)]$ integrated similarly.

Direct reflection: ρ_B Distribution given by Monte Carlo simulations, used here for checks (see below) but really resolves as $\rho_B = \epsilon_{\text{SESR}} + \rho_{\text{SRSR}}$.

Energy conservation implies the following:

$$(\epsilon_A + \epsilon_B) = 1 - (\rho_A + \rho_B) \qquad (4.1)$$

or, equivalently,

$$(\epsilon_A + \epsilon_B + \epsilon_{\text{SESR}}) = 1 - (\rho_A + \rho_{\text{SRSR}}). \qquad (4.2)$$

These equalities are satisfied in the present results.

To test the sensitivity to the steepness of the sea, that is, the cutoff angle for the secondary reflectance contributions, the above terms are defined for $\theta_{\text{cutoff}} = 85°$ and $90°$; in the following, a subscript 85 or 90 indicates this where necessary.

5. Effect on ATSR brightness temperatures

In this section we assess the effect of the various emission and reflection terms by their effect on the brightness temperatures measured by ATSR under various atmospheric conditions. In particular, we wish to examine departures from the simplest situation to model, that of constant emissivity and specular reflection or CESR.

Three widely differing atmospheric temperature and humidity profiles were chosen from a large global set of radiosondes. They essentially represent what we may call *wet, medium,* and *dry* profiles with total water contents of 5.92, 2.84, and 1.40 cm, respectively. The ATSR channel transmittances (at 55°) τ_s for each profile are given in Table 2. They have been calculated

using an accurate line-by-line model developed especially for ATSR (Zavody 1994).

The brightness temperatures presented in this section are not calculated exactly using the full line-by-line model. Instead, we use the following simplified radiative transfer equation

$$I = B(T_s)\epsilon\tau_s + B(T_a)(1 - \tau_s) + \tau_s\rho I^{\downarrow}, \qquad (5.1)$$

where I is the total radiance given by an atmosphere with a surface temperature T_s, lower-layer temperature T_a, and that has downwelling radiances $I^{\downarrow}$. The channel transmittances, emissivities, and reflectivities are τ_s, ϵ, and ρ, respectively. The first term on the right-hand side is the surface-emitted radiance, the second term is an approximation to the radiance emitted from the atmosphere, and the last is the reflected downwelling radiance. We calculate brightness temperatures from I using the inverse Planck function with channel central wavenumbers; this is sufficiently accurate for the present purposes. In the following results the surface emission and reflection terms are obtained by various formulations of ϵ, ρ, and $I^{\downarrow}$. The atmospheric emission term is independent of the variables we wish to test, justifying the use of an approximation here.

The downwelling radiances were calculated using the line-by-line model; an example is given in Fig. 8 that is for the 12-μm channel. The reflection lobe for a 15 m s^{-1} wind is also shown.

The radiances plotted are normalized to be a maximum at the horizon and clearly show strong variation, at least in the drier atmospheres, with zenith angle. The plot shows the significant below horizon reflection and the displacement of the lobe to a zenith angle higher than the specular reflection angle, suggesting that the specular reflection approximation could lead to errors.

a. Emissivity

Figure 9 examines purely the effect of the SESR emission—no reflected sky radiance is included—on the 12-μm channel brightness temperatures in a dry atmosphere. If only direct emission is modeled, the brightness temperatures fall significantly with increasing wind speed by about 0.6 K over the total range. Inclusion of SESR emission halts this fall off as the wind reaches 5–10 m s^{-1}, the difference between inclusion and omission of SESR emission is up to 0.4 K

TABLE 2. Characteristics of the three test atmospheric profiles.

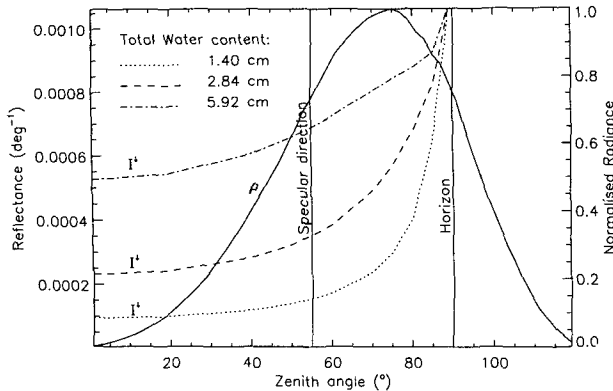| Profile	Wet	Med	Dry
Transmittance τ_s 3.7 μm (%)	62.5	74.5	82.1
Transmittance τ_s 11 μm (%)	18.3	56.0	84.0
Transmittance τ_s 12 μm (%)	8.1	41.8	76.5
Total water (cm)	5.92	2.84	1.40
Surface temperature T_S (K)	301.8	296.4	273.6
Lower-atmosphere temp T_a (K)	293.0	290.0	270.0

FIG. 8. Zenith angle dependence of the rough sea reflectance and downwelling sky radiances for the 12-μm channel at the 55° forward view angle. A wind speed of 15 m s^{-1} was used. The reflectance ρ per degree is shown by the solid line and the radiance profiles $I^{\downarrow}$ normalized and in arbitrary units, are for the three test atmospheric profiles.
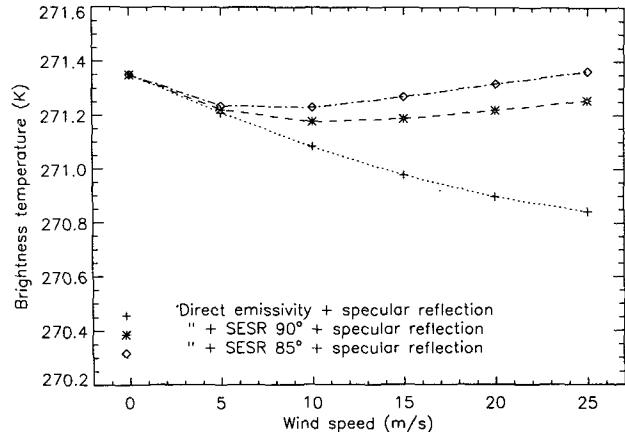

FIG. 10. The 12-μm channel brightness temperatures as in Fig. 9 but including specular reflection of downwelling radiation at 55° calculated from the dry atmosphere.

at high wind speeds. The difference caused by the 90° or 85° cutoff angles is around 0.1 K.

With the moister profiles the behavior of the various curves are similar to those shown in Fig. 9, but the scales of the effects are all smaller as the atmosphere becomes more opaque, and the surface effects are therefore less important. In the wet atmosphere case the 12-μm channel barely sees the surface (see Table 2) and deficits are negligible (<0.1 K).

b. Reflection

All these differences are reduced, albeit only slightly, if we include a specular reflection contribu-

tion; lowering emissivity implies higher reflection and therefore some (although, in an optically thin atmosphere, not much) reduction of emission deficits. In Fig. 10, the appropriate specular reflection term has been added; that is, in (5.1) we have taken $I^{\downarrow}$ to be $I^{\downarrow}(55°)$ and ρ to be $(1 - \epsilon)$.

We can, however, calculate the reflected component exactly by integration of the downward radiance over the reflectance lobe: $\int_\theta \rho(\theta)I^{\downarrow}(\theta)d\theta$. The upper limit of integration is 90° if the emission used was direct only or SESR$_{90}$ and 85° if the emission used was SESR$_{85}$. Figure 11 shows that although the increment caused by SESR emission remains, the distinction between the two cutoff angles is reduced. This occurs because the sky brightness near the horizon tends to be close to the surface temperature so that the surface emission in the 5° near-grazing incidence is very similar to the sky ra-
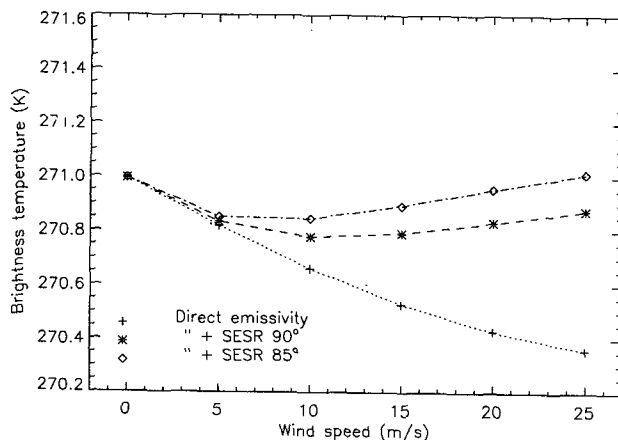

FIG. 9. The 12-μm channel brightness temperatures calculated using Eq. (5.1) excluding the reflected sky radiance component and employing three different formulations of the emissivity: direct only, direct + SESR$_{90}$, and direct + SESR$_{85}$. Atmospheric transmittances calculated from the dry (1.40 cm of precipitable water) profile were used.
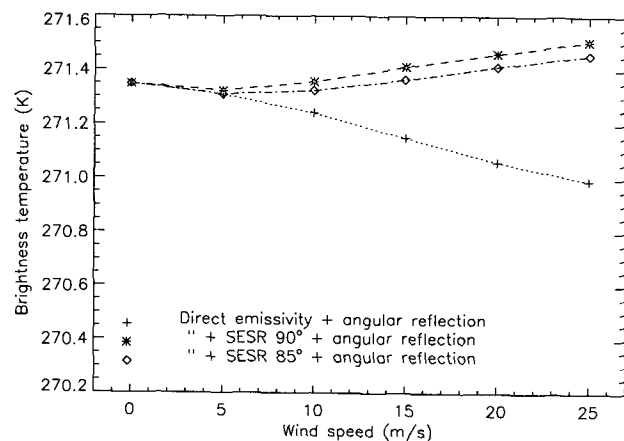

FIG. 11. The 12-μm channel brightness temperatures as in Fig. 9 but including reflection calculated exactly by angular integration of the downwelling sky radiance.
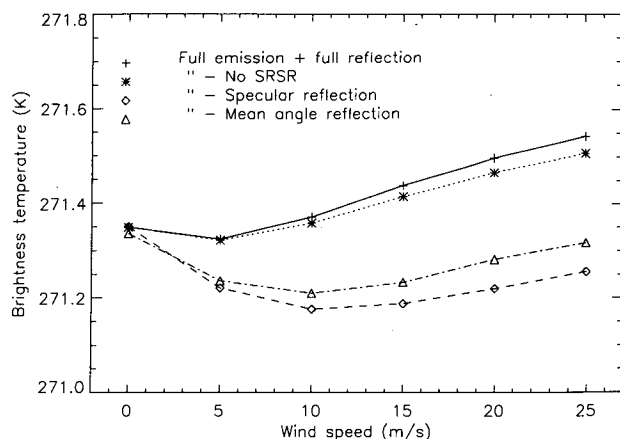
FIG. 12. The 12-μm channel brightness temperatures calculated using Eq. (5.1) with emissivity given by the direct + SESR$_{90}$ formulation and reflection given by various formulations: exact reflection from angular integration of the downwelling sky radiance and including SRSR radiation; similarly, but without the SRSR radiation; using specular reflection at the view angle; using specular reflection at the mean angle of the reflection lobe.

diance. This is encouraging only in the sense that it means that what ATSR actually measures is not strongly affected by the sea steepness. Figure 10 emphasizes that a feasible fast model (i.e., specular reflection using a variable emissivity) is sensitive to the cutoff angle albeit only to a somewhat marginal 0.1 K.

The broad nature of the reflection lobes suggests that modeling reflection as specular may lead to errors. Here, we show the effect of various reflectance models on the resulting brightness temperatures directly. The emission for all plots includes SESR$_{90}$. Figure 12, again for the 12-μm channel and the dry atmosphere, shows four lines. The solid line gives the brightness temperatures calculated using exact integration of the reflectance profile $\rho = \int_\theta \rho(\theta) I^\downarrow(\theta) d\theta$, with an upper integration limit of 90° in this case and the $\rho(\theta)$ including the enhancement due to SRSR radiation. The dotted line shows that the effect of ignoring the SRSR enhancement is quite small, reaching only about 0.05 K.

The specular reflection approximation, $\rho = (1 - \epsilon)I^\downarrow(55°)$, clearly shows a significant deficit for wind speeds above 5 m s^{-1}. This occurs because the reflection lobe is peaked at a higher zenith angle than the specular direction and because of contributions from the high sky brightness near the horizon. The mean angle approximation $\rho = (1 - \epsilon)I^\downarrow(\theta_{mean})$, where θ_{mean} is the mean angle of the part of the reflection lobe that is above the (90°) horizon leaves a significant deficit. The deficit is therefore principally caused by the high near-horizon sky brightness.

As before, the effects shown above depend in magnitude on the channel and the total column water; for the 12-μm channel in the wet profile the differences between reflectance formulations are very small (<0.03 K).

c. Net wind speed effect

Here we discuss the overall effect of wind speed–dependent emission and reflection. From section 5a we saw a reduction in radiance due to falling emissivity with wind speed, although the SESR contribution prevents this becoming large. In section 5b, however, we see an enhancement in radiance due to the wide reflection lobe, and a conclusion of section 5b was that assuming specular reflection would lead to deficit in the predicted radiance. The separate conclusions are that assuming a constant emissivity leads to overestimation of the radiance and assuming specular reflection leads to underestimation of the radiance. Looking again at Fig. 12 we see that, for this single case at least, the two effects cancel to a large extent—the change in brightness temperature over the whole wind speed range amounts to only 0.1 K—and that the brightness temperature at high winds is higher than that at low winds. If this result is consistent for all situations (i.e., combinations of wind speed and atmospheric opacity), then the CESR approximation is, after all, likely to be sufficiently accurate for most purposes. We test this here by calculating radiances for a diverse set of 32 profiles and accumulating the mean and variance of the departure of the CESR approximation from the true radiance. The CESR values are obtained using the zero wind speed emissivity including SESR$_{90}$, and the downwelling radiance at 55°. True radiances are obtained using wind speed–dependent emissivities (including SESR$_{90}$) and angular integration of the downwelling radiance to the 90° horizon. Figure 13 shows the mean and standard deviation of this residual for the three channels.

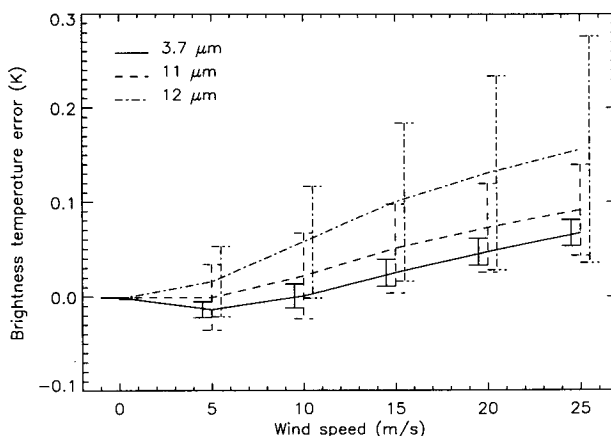Even for the 12-μm channel, which suffers the largest errors, we see that the canceling of enhanced re-

FIG. 13. Statistics of the brightness temperature difference, true minus CESR approximation for 32 profiles with diverse water contents, see text for details. Mean differences are plotted, and standard deviations shown by the error bars that are staggered in channel for clarity.

flection and reduced emission keeps the CESR approximation error to about or below 0.1 K. We should note that, contrary to various reports in the literature that do not consider SESR radiation and/or assume specular reflection (e.g., Masuda et al. 1988; Harris et al. 1994; Coll and Caselles 1993), the CESR approximation will actually slightly underestimate the radiance observed in most conditions; that is, the radiance from the sea surface normally increases with increasing roughness, a conclusion that agrees with the early results of Saunders (1968).

For most purposes then, we can say that the approximation of using a constant sea surface emissivity and specular reflection does not often give rise to significant errors in the calculation of ATSR forward view radiances for reasonable wind speeds. Nevertheless, the CESR approximation can be improved upon if wind speed and atmospheric information is available, and section 6 discusses fast models of the emission and reflection.

6. Parameterizing emissivity and reflectivity

Guissard et al. (1993) used a factor δ to account for the change in microwave (5–40 GHz) reflectivity from the specular approximation. Factor δ was parameterized successfully in terms of the total atmospheric attenuation in the specular direction and the friction velocity. Petty and Katsaros (1993) working in the 19–85-GHz region of SSM/I, parameterized deviation of emissivity from the flat surface Fresnel value in terms of the effective slope variance g^2, the view angle, and the surface temperature. They treated rough surface reflectivity by finding an effective specular reflection angle. The deviation of this from the view angle was modeled in terms of g^2, the view angle, and the atmospheric optical depth. The relatively large rough surface effects in the microwave region (up to 10 K, Petty and Katsaros 1993) demanded this treatment.

From section 5 it appears that the most significant deviations from a CESR model in the wavelength region of ATSR are due to the extent of the reflection lobe and not to variations in the emissivity. The decrease in direct emissivity with wind speed is mostly offset by the secondary emission (SESR) term to leave a small variation of less than 0.2 K under most conditions. The ambiguity that results from determining the cutoff value for θ_s is up to 0.1 K if a CESR model is used. The largest errors, however, arise from the reflection term, with deficits up to 0.3 K when no allowance is made for near-horizon sky brightness.

The variation in emissivity is only a function of the wind speed and therefore is somewhat easier to model than variation in reflectivity that varies with both wind speed and the characteristic sky radiance field.

a. Emissivity parameterization

We have employed a sea surface emissivity model of the form

$$\epsilon_{\text{nadir view}}(\theta, \lambda) = \epsilon_F(0, \lambda) \tag{6.1}$$

$$\epsilon_{\text{forward view}}(\theta, \lambda) = E(\theta, \lambda, W), \tag{6.2}$$

where $\epsilon_F(0, \lambda)$ is the flat surface fresnel emissivity for zero zenith angle and E is a parameterization of the preceding results; we have used a quadratic fit in W and θ. This takes the form

$$E(\theta, \lambda, W) = C_{0,0} + C_{1,0}W + C_{2,0}W^2$$
$$+ C_{0,1}\theta + C_{0,2}\theta^2 + C_{1,1}W\theta + C_{2,1}W^2\theta$$
$$+ C_{1,2}W\theta^2 + C_{2,2}W^2\theta^2, \tag{6.3}$$

where W and θ are expressed in meters per second and degrees, respectively, and the coefficients C implicitly depend on λ and are valid only in the range $0 < W < 25 \text{ m s}^{-1}$ and $52° < \theta < 55°$. Values of the coefficients for all channels and the three formulations of emissivity are given in appendix D. Figures 14 and 15 show the emissivity variation with wind speed and view angle (solid line) and the fitted values (dashed line). Figure 14 is for the direct-only emissivity that is seen to fall systematically with wind speed. The fit in this case is very close. The more interesting case of emission with SESR radiation (85° in this case) where the falloff with wind speed is arrested is shown in Fig. 15. The fit is poorer here but still more than adequate for what is already a small effect.

b. Reflectivity parameterization

The parameterization of reflectivity has the complication that it is also a function of the sky radiance distribution that is strictly a function of the vertical structure of the atmosphere pertaining at the time of the sounding. Here, however, we find we can adequately model the reflectance enhancement due to sky radiance in terms of the wind speed and τ_s, the surface to space
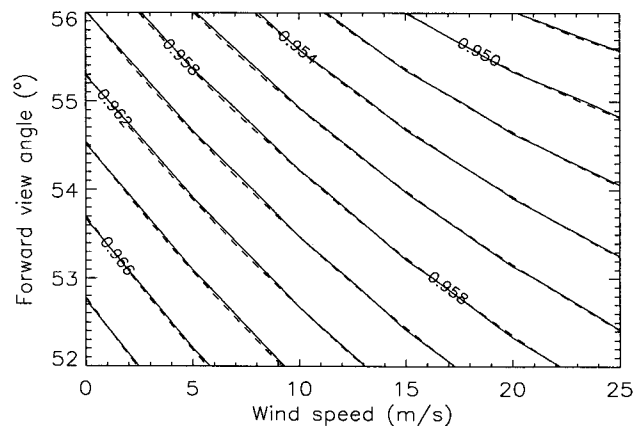

FIG. 14. Two-parameter fit to the direct emissivity in the 12-μm channel. Solid lines show the calculated emissivity, dashed lines show the fitted values obtained from Eq. (6.3), coefficients for which are given in appendix D.

FIG. 15. Two-parameter fit to the direct + SESR$_{85}$ emissivity in the 12-μm channel. Solid lines show the calculated emissivity and dashed lines show the fitted values obtained from Eq. (6.3), coefficients for which are given in appendix D.
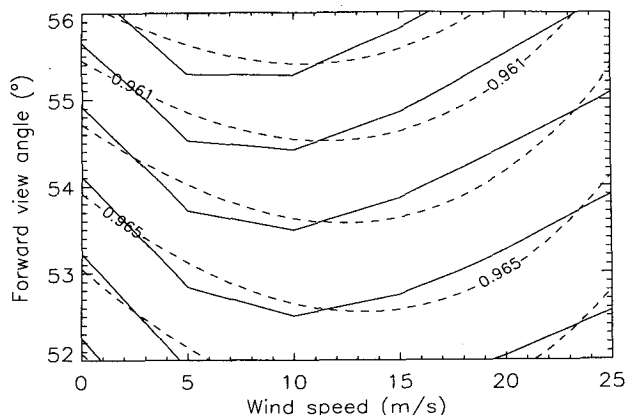
atmospheric transmittance at the specular direction. Here τ_s is principally a function of the atmospheric water content and thus to a large extent determines the zenith sky radiance dependence. It is a suitable parameterization in the context of physical retrievals from ATSR where integration of the radiative transfer equation, and therefore τ_s, is an integral part of the process. For other applications or methods it may make better sense to use a parameterization in terms of the total water content. The attractive method of finding an effective specular angle (e.g., Petty and Katsaros 1993) is not used, because it implies the need to calculate downwelling radiances at two angles, effectively doubling the computation time of any fast model calculation.

The approach taken here is to preserve the CESR (constant emissivity/specular reflection) model because of its simplicity and speed [the sky radiance at the specular direction is available (at least to a good approximation) from the upward transmittance calculation required in a physical retrieval scheme] and to parameterize the enhancement to the reflection above the CESR value. We can express the enhancement of reflected radiance as a factor

$$F = \frac{\displaystyle\int_\theta \rho(\theta)I^\downarrow(\theta)d\theta}{I^\downarrow(55°)\displaystyle\int_\theta \rho(\theta)d\theta}, \qquad (6.4)$$

where the numerator is the true reflectance and the denominator is the specular approximation for a 55° view angle. Factor F is in general a function of channel, wind speed, and atmospheric conditions. Figure 16 shows F (as lines) as a function of wind speed for the 3.7-μm channel under the three varied atmospheres. At zero wind the enhancement is practically unity. (There is a

small effect as the lobe has still a finite width.) At higher wind speeds the enhancement reaches up to 1.7 in the dry atmosphere but reaches lower values in wetter atmospheres where the sky radiance increases less dramatically toward the horizon. This dependency on atmosphere is stronger in the more opaque 12-μm channel. In this case there is virtually no enhancement in the case of the wet atmosphere.

The accompanying symbols mark the fit made to F by the following parameterization in terms of τ_s and the wind speed w:

$$F = [A - Be^{(-w/C)}]\tau_s^D + E. \qquad (6.5)$$

The coefficients for each channel are given in appendix D. Two sets are given: one appropriate to a cutoff angle of 90° and one to 85°. The procedure, therefore, to obtain the reflected radiance is to calculate the downward radiance in the specular direction by normal integration of the radiative transfer equation and then to multiply it by the factor F given estimates of wind speed and τ_s.

The results given above show the fit for the atmospheric profiles used to determine the coefficients. To test the fit on independent data we choose three more profiles with characteristics given in Table 3 and apply (6.5) as before. The fit for the 12-μm channel is shown in Fig. 17 for the 90° case to be quite adequate. The other channels are equally accurately fitted. We performed similar checks to show that the factors derived for the reflection enhancement at 55° are appropriate at other angles (52°–56°).

7. Summary and conclusions

A detailed study of the sea surface emissivity and reflectance has been made using the direction-indepen-

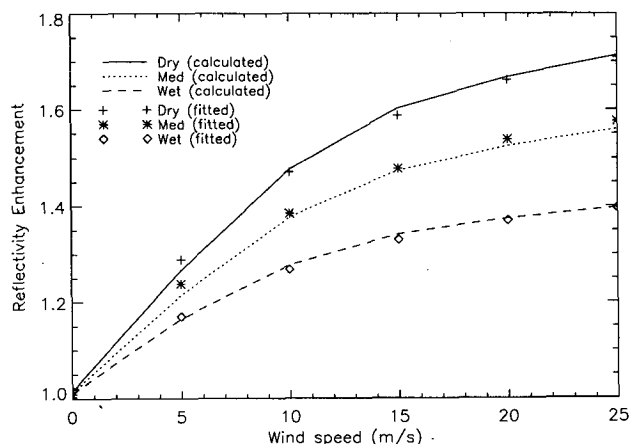FIG. 16. Two-parameter fit to the reflectance enhancement factor F for a 55° view angle in the 3.7-μm channel and for the three test profiles. The lines give the F values obtained by calculation; the symbols give the fitted values using Eq. (6.5), coefficients for which are given in appendix D. The coefficients are optimized to the three test profiles and using F values calculated for a 55° view angle.

TABLE 3. Characteristics of the three independent
atmospheric profiles.

Independent profile	1	2	3
Transmittance τ_s 3.7 μm (%)	86.85	76.02	67.89
Transmittance τ_s 11 μm (%)	93.42	68.95	35.06
Transmittance τ_s 12 μm (%)	90.95	56.71	21.04
Total water (cm)	0.579	2.440	4.402
Surface temp T_s (K)	270.18	281.70	300.32
Lower-atmosphere temp T_a (K)	266.0	276.0	290.0

dent version of the Cox and Munk wind speed–dependent slope distribution. At low zenith angles, that is, near nadir viewing, emission and reflection from the sea are not appreciable functions of the sea state. However, at view angles typical of the ATSR forward view, that is, approximately 55°, significant effects become apparent. We first reproduce the results of Masuda et al. (1988) for the direct emission from a rough sea. The emissivity in all channels falls significantly as the wind speed increases.

We then model the effect of radiation emitted from the surface and reflected into the satellite view direction (SESR). For the ATSR forward view this effect becomes significant when sea slopes of about 15° become frequent, that is, when the wind speed reaches 5 m s^{-1}. We used the direct emission calculations from the Cox and Munk model to obtain the emission at high zenith angles, that is the radiance field expected within the wave troughs of the sea. We then "reflected" this field by each facet that was so sloped as to receive radiation from below the "horizon" and reflect it toward the satellite. The definition of the horizon is open to question as it depends to some extent on the steepness of the sea. Calculations including this formulation of SESR give emissivities that do not drop for wind speeds above 5–10 m s^{-1}.

Using a simplified radiative transfer model and three diverse atmospheric profiles we find that without the SESR contribution included, measured brightness temperatures typically might fall by up to 0.5 K with increasing wind speed, depending on the opacity of the atmosphere and the channel concerned. However, if the SESR radiation is included, the fall in brightness temperature is at most 0.2 K (less if the higher horizon is assumed) followed by a leveling off with higher winds.

Concerning the behavior of reflected radiation, we obtained the reflection lobes for a rough sea using a Monte Carlo method. This clearly showed that the lobe width increased with wind speed, the peak moving to higher angles than the specular direction and part of the lobe dipping below the horizon for wind speeds above 5 m s^{-1}. This latter point is related to the SESR emission and led to evaluation of a second multiple reflection effect, SRSR reflection. Although the angular distribution of SRSR radiation was not obtained, the total contribution was estimated and was found to be about

5% of the total reflectivity, making it a rather small effect.

By means of the simplified radiative transfer model and precise calculations of the downward sky radiance field, we estimated the effect on brightness temperatures of the reflection lobe, particularly how detailed calculations of reflection would differ from the simple specular approximation. It was found that, particularly because of the high sky radiance near the horizon, the specular reflection approximation would give a deficit of up to 0.3 K, again dependent on the atmospheric opacity and channel concerned. The contribution of SRSR radiation was, as expected, negligible.

Thus, we find the assumption of constant zero wind speed emissivity and specular reflection (CESR) leads to an overestimate of emitted radiance but an underestimate of reflected radiance at the higher wind speeds. We find the net effect to be rather small—<0.1 ± 0.1 K—and conclude that, for most purposes, the CESR approximation is an adequate approximation at all wind speeds. We also noted that the net effect is positive, that is, that the radiance from a sea surface normally increases slightly as the surface roughens.

The validity of these theoretical results needs to be confirmed by experiment. In this respect, the method of Francois and Ottle (1994) is promising and confirms the predicted angular dependence of emissivity. The same authors have extended their analysis to the wind speed dependence and their preliminary findings seem to show a slight decrease in emissivity with wind speed for low winds (<6 m s^{-1}) as expected from this work (Ottle 1995, personal communication). Future field campaigns will use a shipborne radiometer built at the Rutherford Appleton Laboratory, matched and intended for ATSR validation studies. Supported by local meteorological and in situ sea surface temperature measurements, it hopefully will provide a database from
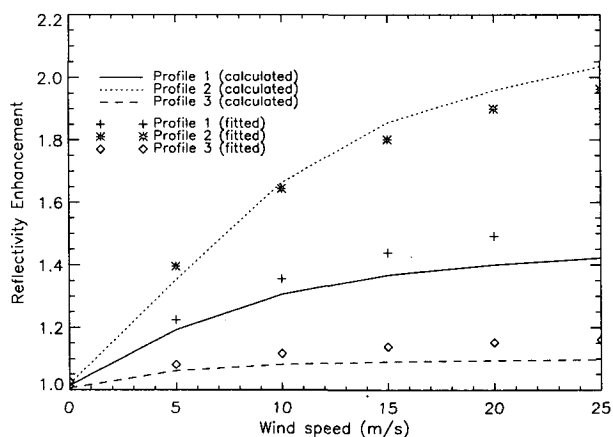

FIG. 17. As in Fig. 16 but for three independent test atmospheric profiles. The coefficients used are as in Fig. 16, that is, obtained from the original three test profiles and with a 55° view angle.

which we can more thoroughly check the results of this paper.

The final section dealt with parameterization of the emission and reflection behavior with a view to fast radiative transfer modeling. The emissivity was fitted to a quadratic form in two variables: wind speed and view angle. Coefficients for this fit were found for emissivity calculated with and without SESR effects and for SESR horizons at 85° and 90°. Parameterization was not made of reflectivity directly but of the enhancement caused by the finite width lobe. In this case the water content, and so the opacity, of the atmosphere is an important factor, and the parameterization is based on wind speed and the surface–top of atmosphere transmittance calculated at the specular angle. The latter effectively determines the degree of variance observed across the sky zenith. Both parameterizations are found to work adequately and fit within the framework of a fast radiative transfer model for ATSR.

APPENDIX A

Zenith and Azimuth Angles of the Specular Direction Vector

The spherical coordinate system used is shown Fig. A1. The vectors $\mathbf{n}$, $\mathbf{i}$, and $\mathbf{s}$ are the normal to the facet plane, the incident ray direction, and the reflected ray direction, respectively. They are given by

$$\mathbf{n} = (\cos\phi_n \sin\theta_n, \sin\phi_n \sin\theta_n, \cos\theta_n),$$

$$\mathbf{i} = (-\sin\theta, 0, -\cos\theta),$$

$$\mathbf{s} = (\cos\phi_s \sin\theta_s, \sin\phi_s \sin\theta_s, \cos\theta_s).$$

First we have

$$\cos\chi = -\mathbf{i}\cdot\mathbf{n} = \cos\theta \cos\theta_n + \cos\phi_n \sin\theta_n \sin\theta.$$
(A.1)

The three vectors are coplanar and moreover $\mathbf{s} - \mathbf{i}$ lies in the $\mathbf{n}$ direction; thus,

$$\mathbf{s} - \mathbf{i} = 2 \cos\chi\mathbf{n},$$

which, separated into components, gives

$$\cos\phi_s \sin\theta_s + \sin\theta = 2 \cos\chi \cos\phi_n \sin\theta_n$$
(*x* component)   (A.2)

$$\sin\phi_s \sin\theta_s = 2 \cos\chi \sin\phi_n \sin\theta_n \quad (y \text{ component})$$
(A.3)

$$\cos\theta_s + \cos\theta = 2 \cos\chi \cos\theta_n \quad (z \text{ component}).$$
(A.4)

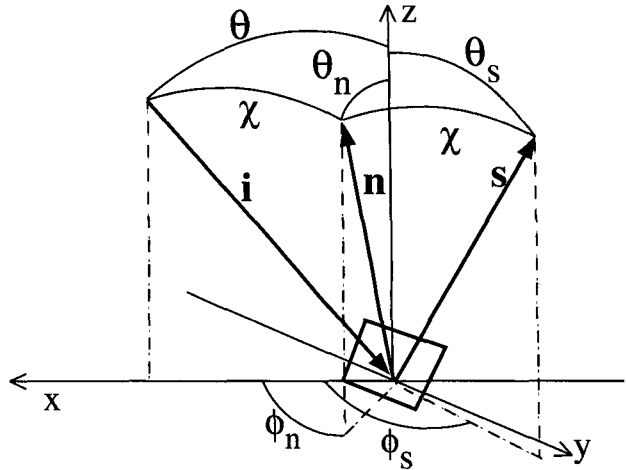Equation (A.4) gives θ_s immediately

FIG. A1. The coordinate system used in the paper. The facet is shown by the small rectangle and has a normal vector $\mathbf{n}$. Unit vectors $-\mathbf{i}$ and $-\mathbf{s}$ are in the direction of the satellite and the reflected ray, respectively.

$$\cos\theta_s = 2 \cos\chi \cos\theta_n - \cos\theta.$$
(A.5)

Equation (A.2) can be written

$$\cos\phi_s \sin\theta_s = 2 \cos\chi \cos\phi_n \sin\theta_n - \sin\theta$$
(A.6)

and (A.6)/(A.3) gives ϕ_s through

$$\cot\phi_s = \cot\phi_n - 1/2 \frac{\sec\chi \sin\theta}{\sin\phi_n \sin\theta_n}.$$
(A.7)

APPENDIX B

Use of a Channel Bandwidth-Averaged Refractive Index

Emissivity calculations should strictly be made using integrations over the channel bandwidth allowing for the variation of complex refractive index $\mathbf{n}$ with wavenumber ν; that is,

$$\epsilon_{\text{true}} = \int_0^\infty f(\nu)\epsilon_F[\mathbf{n}(\nu)]d\nu,$$
(B.1)

where $f(\nu)$ is the normalized filter response function.

However, to reduce the considerable computation that this would require, we use the value of $\mathbf{n}$ at the mean channel wavenumber ν_m defined by

$$\nu_m = \int_0^\infty f(\nu)\nu d\nu.$$
(B.2)

Thus,

$$\epsilon_m = \epsilon_F[\mathbf{n}(\nu_m)].$$
(B.3)

Table B1 compares ATSR channel emissivities for a flat water surface calculated exactly using (B.1) and approximately using (B.3) and at a wide range of an-

TABLE B1. Mean wavenumbers and refractive indicies for the three ATSR thermal channels and flat surface Fresnel emissivities resulting from their use compared with true values.

θ	Channel	3.7 μm	11 μm	12 μm
	Mean wavenumber ν_m (cm^{-1})	2690.45	916.63	840.13
	Refractive index (real) of water at wavenumber ν_m	1.3784	1.1569	1.1572
	Refractive index (imaginary) of water at wavenumber ν_m	0.0040036	0.096359	0.198673
10°	ϵ_{true}	0.9744	0.9922	0.9862
	ϵ_m	0.9747	0.9927	0.9863
55°	ϵ_{true}	0.9490	0.9777	0.9634
	ϵ_m	0.9494	0.9789	0.9633
80°	ϵ_{true}	0.6381	0.7064	0.6475
	ϵ_m	0.6388	0.7122	0.6565

gles. Refractive index data were taken from the review made by Irvine and Pollock (1969).

The largest error of 0.1% appears in the 11-μm channel at 55°. From the results presented earlier in this paper we can conclude that this does not represent a significant error.

APPENDIX C

The Effect of Sea Foam

Mention here is made of the "contamination" of the pure sea state with foam: whitecaps from breaking waves and foam streaks. Measurements by Ross and Cardone (1974) suggest the estimates of total foam coverage with wind speed for unlimited fetch given in Table C1. The variance about these figures is likely to be quite high.

Estimating the effect of this foam on the emissivity is difficult, since theories on the subject seem to be unavailable and measurements are very sparse. At least two theoretical methods and numerous empirical studies for the microwave region are in the literature (Ulaby et al. 1986). These may be adaptable to the infrared but are complicated because the wavelength of the microwaves is comparable to the bubble size and much longer than the water film thickness. In the infrared, the wavelength is much shorter than bubble size and greater than the film (films are order 1 μm thick) and a simpler analysis may pertain. The microwave results indicate an increase in emissivity for foam over an unbroken surface.

Measurements of hemispherical reflectivity of seawater and foam made by Salisbury et al. (1993) show that in the 8–12-μm region at least, this parameter is unaffected by the presence of foam. Salisbury et al. conclude that, unlike in the visible wavelength region,

the film thickness and high absorption in the infrared prevent significant volume scattering and therefore any change in emissivity over a "solid" water surface. It seems plausible then that the only change foam can make is by virtue of it altering the slope distribution observed. A "worst" case situation is that foam takes on an emissivity as high as the nadir-viewed flat surface value (worst in the sense that the largest deviation from the relatively predictable unbroken sea surface emissivity is obtained). Figure C1 shows the effect of foam of this emissivity with the above fractional coverage f; that is,

$$\epsilon(55°, f) = \epsilon(55°, 0)(1 - f) + \epsilon(0°, 0)f. \quad (C.1)$$

The direct-only emissivity has been used for $\epsilon(0)$ here. In this extreme case the presence of foam invalidates the foam-free emissivity model for the forward view for $W > 15$ m s^{-1}; the nadir view values are unchanged.

APPENDIX D

Coefficients for the Emissivity and Reflectivity Parameterizations

The coefficients found for the quadratic emissivity fit given in (6.3) are tabulated below in the order

$$\begin{array}{ccc} C_{0,0} & C_{1,0} & C_{2,0} \\ C_{0,1} & C_{1,1} & C_{2,1} \\ C_{0,2} & C_{1,2} & C_{2,2}. \end{array}$$

The coefficients are valid for $0 < W < 25$ m s^{-1} and $52° < \theta < 55°$.

3.7-μm channel. Type: direct only

TABLE C1. Foam cover as a function of wind speed from Ross and Cardone (1974).

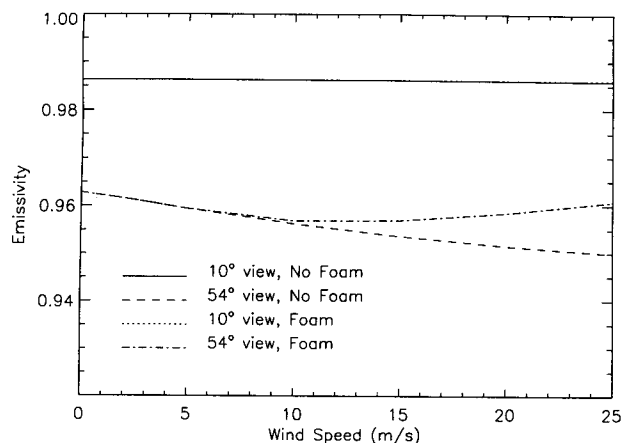| Wind speed (m s^{-1})	0	5	10	15	20	25
Foam cover	0%	0%	2%	10%	20%	30%

FIG. C1. Calculated effect of foam on the direct emissivity. The foam is assumed to have emissivity equal to that of flat water surface at nadir view (12-μm channel). Foam cover fractions are taken from Ross and Cardone (1974).

7.225207e − 01	3.626517e − 04	2.865613e − 04
1.095384e − 02	6.828484e − 06	−1.202583e − 05
−1.243110e − 04	−5.009081e − 07	1.275904e − 07

11-μm channel. Type: direct only

8.074828e − 01	−3.825370e − 03	3.537125e − 04
7.888448e − 03	1.764039e − 04	−1.450966e − 05
−8.686313e − 05	−2.154383e − 06	1.493825e − 07

12-μm channel. Type: direct only

7.252373e − 01	5.097713e − 04	3.066133e − 04
1.125498e − 02	2.415080e − 05	−1.289790e − 05
−1.260950e − 04	−7.271655e − 07	1.3695998e − 07

3.7-μm channel. Type: direct + SESR$_{90}$

7.201142e − 01	6.985957e − 03	−9.139763e − 05
1.109264e − 02	−2.825062e − 04	3.078423e − 06
−1.261832e − 04	2.645058e − 06	−1.885155e − 08

11-μm channel. Type: direct + SESR$_{90}$

8.030360e − 01	3.283983e − 03	−1.927707e − 08
8.097693e − 03	−1.240698e − 04	−5.822254e − 07
−8.931088e − 05	1.016176e − 06	1.574042e − 08

12-μm channel. Type: direct + SESR$_{90}$

7.223365e − 01	7.095220e − 03	−7.985249e − 05
1.141268e − 02	−2.804089e − 04	2.470029e − 06
−1.281435e − 04	2.553486e − 06	−1.148004e − 08

3.7-μm channel. Type: direct + SESR$_{85}$

7.197855e − 01	1.651337e − 02	−3.253059e − 04
1.110426e − 02	−6.535705e − 04	1.230272e − 05
−1.263407e − 04	6.306912e − 06	−1.100467e − 07

11-μm channel. Type: direct + SESR$_{85}$

8.029003e − 01	1.058051e − 02	−1.864108e − 04
8.103273e − 03	−4.085382e − 04	6.732609e − 06
−8.940500e − 05	3.821904e − 06	−5.625043e − 08

12-μm channel. Type: direct + SESR$_{85}$

7.220166e − 01	1.621401e − 02	−3.055979e − 04
1.142483e − 02	−6.358377e − 04	1.135790e − 05
−1.283098e − 04	6.061493e − 06	−9.920226e − 08

The ATSR channel emissivities for the nadir view ($\theta < 30°$) can be taken to be constant with value equal to the plane surface Fresnel emissivity. They are given in the following table.

ATSR nadir emissivities

3.7 μm	11 μm	12 μm
0.9746	0.9927	0.9863

The enhancement factor to specular reflection is parameterized as follows:

$$F = [A − Be^{(-w/C)}]\tau_s^D + E.$$

The coefficients for the fit for a cutoff angle of $\theta_s > 90°$ are given in the following table.

$\theta_s > 90°$	3.7 μm	11 μm	12 μm
A	1.20871	1.80931	1.16434
B	−1.25127	−1.90780	−1.19625
C	−11.5626	−12.1488	−11.2019
D	2.26850	2.10138	1.34632
E	1.03099	1.06648	1.02928

For $\theta_s > 85°$ we find the following.

$\theta_s > 85°$	3.7 μm	11 μm	12 μm
A	0.445255	0.652266	0.511694
B	−0.458377	−0.654097	−0.491494
C	5.09645	−5.71811	−5.32790
D	2.04670	1.60560	1.28030
E	1.02092	1.02113	1.00425

REFERENCES

Coll, C., and V. Caselles, 1994: Analysis of the atmospheric and emissivity influence on the split-window equation for sea-surface temperature. *Int. J. Remote Sens.,* **15,** 1915–1932.

Cox, C., and W. Munk, 1954: Measurements of the roughness of the sea surface from photographs of the sun's glitter. *J. Opt. Soc. Amer.,* **44,** 838–850.

Edwards, T., and Coauthors, 1990: The Along Track Scanning Radiometer measurement of sea-surface temperature from ERS-1. *J. Br. Interplanet. Soc.,* **43,** 160–180.

Francois, C., and C. Ottle, 1994: Estimation of the angular variation of the sea surface emissivity with the ATSR/ERS-1 data. *Remote Sens. Environ.,* **48,** 302–308.

Guissard, A., and P. Sobieski, 1987: An approximate model for the microwave brightness temperature of the sea. *Int. J. Remote. Sens.,* **8,** 1607–1627.

——, ——, and A. Laloux, 1993: Radiative transfer equation with surface scattering for ocean and atmospheric parameters retrieval from radiometric measurements. *Int. J. Remote. Sens.,* **15,** 1743–1760.

Harris, A. R., S. J. Brown, and I. M. Mason, 1994: The effect of windspeed on sea surface temperature retrieval from space. *Geophys. Res. Lett.,* **21,** 1715–1718.

Irvine, W. M., and J. B. Pollock, 1968: Infrared optical properties of water and ice spheres. *Icarus,* **8,** 324–360.

Kinsman, B., 1984: *Wind Waves: Their Generation and Propogation at the Surface.* Dover, 676 pp.

Masuda, K., T. Takashima, and Y. Takayama, 1988: Emissivity of pure and sea waters for the model sea surface in the infrared window regions. *Remote Sens. Environ.,* **24,** 313–329.

Michell, J. H., 1893: The highest waves in the water. *Philos. Mag.,* **36**(222), 351–358.

Neumann, G., 1954: Zur characteristich des seeganges. *Arch. Meteorol. Geophys. Bioklimatol.,* **7.**

Otterman, J., J. Susskind, G. Dalu, D. Kratz, and I. L. Goldberg, 1992: Effects of water emission anisotrophy on multispectral remote sensing at thermal wavelengths of ocean temperature and of cirrus clouds. *Appl. Opt.,* **31,** 7633–7646.

Petty, G. W., and K. B. Katsaros, 1993: The response of the SSM/I to the marine environment. Part II: A parameterisation of the effect of the sea surface slope distribution on emission and reflection. *J. Atmos. Oceanic Technol.,* **11,** 617–628.

Ross, D. B., and V. Cardone, 1974: Observations of oceanic whitecaps and their relation to remote measurements of surface wind speed. *J. Geophys. Res.,* **79,** 444–452.

Saunders, P. M., 1968: Radiance of sea and sky· in the infrared window 800–1200 cm⁻¹. *J. Opt. Soc. Amer.,* **58,** 645–652.

Salisbury, J. W., D. M. D'Aria, and F. F. Sabins Jr., 1993: Thermal infrared remote sensing of crude oil slicks. *Remote Sens. Environ.,* **45,** 225–231.

Sidrin, M., 1981: Broadband reflectance and emissivity of specular and rough water surfaces. *Appl. Opt.,* **20,** 3176–3183.

Ulaby, F. T., R. K. Moore, and A. K. Fung, 1986: *Microwave Remote Sensing, Active and Passive Vol III: From Theory to Applications.* Section 18-3.2, Artech House Inc., 2162 pp.

Wentz, F. J., 1983: A model function for ocean microwave brightness temperatures. *J. Geophys. Res.,* **88,** 1892–1908.

Wilheit, T. T., 1979: A model for the microwave emissivity of the ocean's surface as a function of wind speed. *IEEE Trans. Geosci. Electron.,* **17,** 244–249.

Zavody, A., 1994: A radiative transfer model for sea surface temperature retrieval for the Along Track Scanning Radiometer (ATSR). *J. Geophys. Res.,* **100**(C1), 937–952.